Article

Numerical Analysis of Propeller Wake Evolution under Different Advance Coefficients

Duo Yu [1,2], Yu Zhao [3], Mei Li [4], Haitian Liu [1,2], Suoxian Yang [1,2] and Liang Wang [1,2,*]

[1] Key Laboratory of Fishery Equipment and Engineering, Ministry of Agriculture and Rural Affairs, Fishery Machinery and Instrument Research Institute, Chinese Academy of Fishery Sciences, Shanghai 200092, China; yuduo@fmiri.ac.cn (D.Y.); liuhaitian@fmiri.ac.cn (H.L.); yangsuoxian@fmiri.ac.cn (S.Y.)
[2] Qingdao National Laboratory for Marine Science and Technology, Qingdao 266237, China
[3] Qingdao Conson Oceantec Valley Development Co., Ltd., Qingdao 266200, China; zhaoyu2023163@126.com
[4] Conson CSSC (Qingdao) Ocean Technology Co., Ltd., Qingdao 266000, China; m13335097920@163.com
[*] Correspondence: liam_wong@126.com

Abstract: Propeller wake fields in an open-water configuration were compared between two loading circumstances using large-eddy simulation (LES) with a computational domain of 48 million grids and an overset mesh technique. To validate the results of the numerical simulation, available experimental data are compared, which indicates that the grid systems are suitable for the present study. The results indicate that the present LES simulations describe the inertial frequency range well for both high and low-loading conditions. Under high-loading conditions, the interlaced spirals and secondary vortices that connect adjacent tip vortices amplify the effects of mutual inductance, ultimately triggering the breakdown of the propeller wake systems. At a great distance from the propeller, the vortex system loses all coherence and turns into a collection of smaller vortices that are equally scattered across the wake. In contrast, under light-loading conditions, the wake vortex system exhibits strong coherence and has a relatively simple topology. The elliptic instability and pairing processes are only observed at a far distance from the propeller. The convection velocity transferring tip vortices downstream is larger under the light-loading condition, which leads to the larger pitch of the helicoidal vortices. The larger pitch weakens the mutual inductance or interaction effects among tip vortices, which delays the instability behaviors of the whole vortex system. The results and implications of this study serve as a guide for the development and improvement of next-generation propellers that function optimally when operating behind aquaculture vessels.

Keywords: marine propeller; numerical simulations; vortex system; LES

1. Introduction

Traditional force and moment analyses have generally provided only a macroscopic perspective of a ship or marine structure performance, offering limited insight into the fundamental interactions and mechanisms between the vessel and its surrounding water particles in complex sea states. This approach has been proven inadequate in helping researchers identify novel directions for performance optimization [1]. Consequently, many researchers now focus on the physical mechanisms and minutiae of fluids to analyze and predict the dynamic and kinematic characteristics of marine structures, fostering innovative design and optimization strategies [2,3]. In response to varying real sea conditions, the propellers of large aquaculture workboats must operate in complex and ever-changing maritime conditions. Environmental factors such as wind, waves, and currents cause significant changes in propeller performance during operation. This necessitates higher performance standards across all aspects of the propeller. An inherent connection exists between the propeller wake and its overall performance. Traditional optimization techniques based on macroscopic data, such as force and moment, struggle to achieve

breakthroughs in hydrodynamic performance and cavitation noise reduction, primarily due to an incomplete understanding of the interaction mechanisms between the propeller and fluids [4,5]. The key to designing high-performance propellers lies within the highly complex fluid dynamics of propeller wakes. To develop propellers with superior comprehensive performance—particularly in terms of noise reduction and greater efficiency—it is essential to analyze the characteristics of propeller wakes. Furthermore, as energy conservation, emissions reduction, and green shipping attract more and more attention, various energy-saving devices are being designed and installed around propellers. The successful implementation of energy-saving appendages can yield considerable economic benefits, with the investigation of propeller wake mechanisms proving critical to the design, development, and application of these devices. The complexity of the propeller wake field determines the difficulty of conducting experimental measurements on it, and the inherent challenges of testing rotating machinery flow fields render traditional methods, such as Pitot tubes, inadequate for capturing effective flow field information. Techniques based on flow visualization have been applied to propeller wake measurements, including methods employing laser-illuminated fluorescent dyes and pressure reduction in a cavitation tunnel to induce vortex cavitation. However, these devices and methods only offer qualitative recordings and observations for the three-dimensional spatial evolution of wake topology and fail to provide quantitative information, thereby imposing certain limitations [6]. Concurrently, dwindling energy resources and new demands for sustainable development in the shipbuilding industry have transformed the mission of ship designers and researchers to design and construct vessels with continuously improving performance. However, evaluating and further optimizing traditional performance attributes of modern marine structures in complex sea conditions, such as maneuverability, and cavitation noise, still face numerous challenges and bottlenecks [7]. As concepts of energy conservation, vibration, noise reduction, and environmental protection in the shipbuilding industry continue to gain traction and become increasingly emphasized, a range of maritime regulations, such as the energy efficiency design index (EEDI), minimum safe power guidelines, and underwater radiated noise guidelines, have been enacted and enforced by the International Maritime Organization (IMO), major classification societies, and other relevant regulatory bodies. Studying propeller wakes from the perspective of flow physics is beneficial for designing and optimizing high-performance propellers to achieve the goals of saving fuel consumption, emission reduction, and green environmental protection, thus meeting modern industry needs and increasingly stringent maritime regulations.

Aquaculture working boats are commonly utilized in deep-sea farming, and although propellers are the vessels' primary propulsion systems, their wake evolution characteristics are of significant interest owing to their link to vibration, noise, and structural issues [8,9]. The flow mechanisms of propeller wakes are extremely complicated and have not been fully understood yet. More knowledge about the flows around propulsors can help people design better propellers used for aquaculture working boats [10,11]. The working conditions of propellers are determined by the non-dimensional parameter J, which is an advance coefficient and computed as $J = \frac{U}{nD}$, where U is the free-stream velocity and n and D are the rotational speed and the diameter of the propeller, respectively. The advance coefficient is related to the propeller loads, and the higher value of J represents the lower loading condition of the propeller.

Common flow problems can generally be studied using theoretical, numerical, and experimental methods. However, it is difficult to obtain analytical solutions for viscous fluid mechanics from a theoretical perspective. Therefore, numerical and experimental studies have many applications in propeller wake studies. Particle image velocimetry (PIV) is often used in the experimental investigation of propeller wakes, since it concurrently measures the detailed flow field information, particularly the velocity field of the whole area, using an optical method. Particle Image Velocimetry (PIV) is a flow field mapping technique that offers a quantitative method for gaining insight into the physical properties of fluid flows. A reference propeller-wing configuration operating with great thickness was

experimentally excavated by Felli [12], where detailed PIV, along with a time-resolved function, was employed for the acquisition of the flow information. The physics or mechanisms behind the propeller flows are not well understood, and flow measures were utilized to investigate the wake–wall interaction within propeller-rudder configurations. The rejoining of vortex lines between the wing border layer and wake vortex cores was influential in maintaining the connection of vortices during the penetration phase. In addition, Capone et al. [13] used PIV to conduct experimental research on wake fields produced by propellers with counter-rotating configurations under varied working circumstances. They found that the aft propeller was more successful at balancing the distribution of the tangential component of certain physical qualities under particular loading situations. In contrast, Wang et al. [14] designed a modified phase-average approach that delivered more realistic vorticity fields than typical phase-average methods using phase-locked analysis. The conventional method of evaluating tip vortex behaviors proved misleading. Their contribution resulted in a potent post-processing tool for analyzing the streamwise development of the flow field. Using a series of flow field measurement equipment, de Vires et al. [15] examined the interaction effects between the flow fields of different propellers. They discovered that active modulation has a pronounced influence on the relative blade motion in the viscous flows.

Technological advancements in computer hardware and software have facilitated the widespread use of numerical approaches in the exploration of propeller wake instabilities. Currently, CFD remains the primary method for calculating viscous propeller wake fields [16], although it faces considerable challenges when studying unsteady characteristics of propeller wakes. Posa et al. [17] analyzed the submarine propeller wakes with varying working conditions. The researchers observed that loading conditions have a significant impact on wake vortices. Posa et al. [18] compared the simulation and PIV test results of a marine propeller, and both Eulerian and Lagrangian approaches functioned as the theoretical basis. Their investigation revealed that the surrounding blades' shear is the primary source of tip vortices' instability. Posa and Broglia [19] investigated the interference between propeller wake vortices evolving upstream of an incidence-oriented rudder. Their studies suggested that the direction of the hydrofoil had a significant influence on propeller flows. Shi et al. [20] studied the duct effects on wake characteristics and instability motions. Transforming high-dimensional complex flow fields into low-dimensional simple flow structures through modal decomposition made it possible to deeply understand the wake fields behind the two different propeller configurations. By comparing different decomposition results, they reported the reasons for the instability of the flow fields of two propellers.

The choice of the CFD method and the associated computational load vary depending on the specific wake characteristics being investigated. For example, when researchers are only concerned with phase-averaged results of the wake field, transient Reynolds-Averaged Navier–Stokes (RANS) methods often yield results that align with PIV experiments. However, when the instability of propeller wakes during their evolution from near-field to far-field becomes the focus, the RANS method proves to be too dissipative and smooths out most of the finest flow features. The intricate vortex structures within this physical process typically necessitate the use of Detached Eddy Simulation (DES) or Large Eddy Simulation (LES) turbulence models to better capture the essential vortex structures, thereby imposing higher requirements on the spatiotemporal resolution of numerical simulations. For instance, accurate simulation of vortex structures with intensities comparable to those observed in experiments becomes difficult when spatial resolution is insufficient in the presence of substantial velocity gradients within vortex cores. Furthermore, CFD methods inevitably entail numerical dissipation, which introduces non-physical factors into the results. Recently, hybrid LES/RANS models such as DES, delayed DES (DDES), and improved DDES (IDDES) have been very popular in propeller wake studies [21–31]. Based on the literature survey presented above, it is evident that there are limited LES studies on propeller wakes under various loading conditions. The main challenge associated with

this research is the high computational cost required to accurately resolve the wake of marine propellers.

This work tries to alleviate this constraint by presenting the LES findings for propellers operating under two loading scenarios. Moreover, this work intends to analyze the flow mechanics that drive the destabilizing processes in the wake under varied loading conditions. Specifically, the wake evolution characteristics are excavated from the three-dimensional vortical structures, the contours of velocity components, the contours of out-of-plane vorticity, and time-averaged quantities under different loading conditions. The inception mechanisms of propeller wake from the stable state to the unstable state are also detailed.

2. Research Model

A four-bladed, right-handed, low-skew, fixed-pitch E779A propeller was used for the numerical approaches. This propeller was first conceived at the CNR-INM for analyzing the performance and wake evolution features of propellers working behind aquaculture working boats. The E779A propeller was selected for two reasons. First, this standard propeller model has been frequently employed in wake instability research due to the availability of abundant reference data from CFD models and PIV testing [32–38], which is convenient for numerical validation. Second, the E779A propeller can generate strong tip vortices in the wake field. Figure 1 depicts the propeller geometry of E779A, including the hub, blades, and rotational orientation. Table 1 lists the key propeller parameters. The geometry model of the propeller can be obtained from GrabCAD at https://grabcad.com/library/e779-marine-propeller-1, accessed on 16 May 2022.
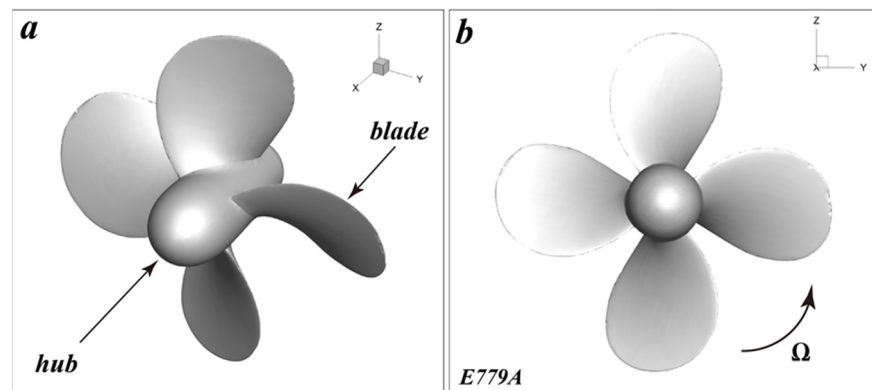

Figure 1. Propeller geometry in the simulated isolated configuration and the coordinate system: (**a**) Oblique view and (**b**) front view. The direction of propeller rotation and blades and hub are labeled.

Table 1. E779A propeller's main parameters.

Quantity	Units	Value
Propeller diameter	mm	227.27
Number of blades	-	4
Pitch ratio	-	1.11
Hub diameter	mm	45.53
Hub ratio	-	0.2
Rake (forward)	-	4°35′
Expanded area ratio	-	0.689
Chord at 0.7R	mm	86

3. Numerical Simulation

3.1. Numerical Method

It may be challenging to ensure the accuracy and trustworthiness of the Reynolds-averaged technique when analyzing the complicated turbulent structures of propeller

wakes. This issue was solved using the LES method, in which flow variables are separated into directly calculable solution scales and sub-grid scales that need modeling through filtering procedures. While LES solves large-scale flow patterns, sub-grid-scale (SGS) models simulate small-scale vortices. Specifically, the WALE SGS model, without any type of near-wall damping, can automatically scale appropriately at solid wall borders. The WALE SGS model is also less susceptible to model coefficients than other current SGS models. The validation of the model in turbulent flow numerical simulations is shown in [39,40]. Notably, the LES approach has been used extensively to examine propeller wake instabilities [17,41], by numerically solving the Navier–Stokes equations with filtered functions:

$$\nabla \cdot \widetilde{\boldsymbol{u}} = 0 \tag{1}$$

$$\frac{\partial \widetilde{\boldsymbol{u}}}{\partial t} + \nabla \cdot \widetilde{\boldsymbol{u}}\widetilde{\boldsymbol{u}} = -\nabla \widetilde{p} - \nabla \cdot \boldsymbol{\tau} + \frac{1}{\mathrm{Re}} \nabla^2 \widetilde{\boldsymbol{u}} \tag{2}$$

where $\boldsymbol{u}$ is the velocity vector, p is the pressure, and Re is the Reynolds number. $\boldsymbol{\tau}$ indicates the subgrid stress tensor:

$$\boldsymbol{\tau} = \widetilde{\boldsymbol{u}\boldsymbol{u}} - \widetilde{\boldsymbol{u}}\widetilde{\boldsymbol{u}} \tag{3}$$

which is modeled using the following equation:

$$\boldsymbol{\tau} = -2\nu_t \widetilde{S} \tag{4}$$

where ν_t is the eddy viscosity and $\widetilde{S}$ is the velocity deformation tensor.

Partial differential equations describing fluid dynamics can be generally solved using commercial software, self-developed programs, or open-source code based on given boundaries and initial conditions. Open-source code is particularly preferred due to its accessibility and versatile functionality. In this study, the OpenFOAM [42,43] was used for calculations. The Navier–Stokes equation was numerically solved using unstructured grids. The overset grid technology has significant advantages in simulating the large-amplitude motion of objects, it achieves data exchange through interpolation of flow field information in different flow regions and has widespread applications in propeller flow field simulation. Utilizing the dynamic overset grid approach [44–47], the propeller of the E779A was made to rotate. The time step was 1.1111×10^4 s, which is small enough to model the motion details and capture the flow structures in the propeller wake. The Reynolds numbers based on the propeller diameter and the free-stream velocities are 4.29×10^5 for the condition of $J = 0.38$ and 7.35×10^5 for the condition of $J = 0.65$, respectively.

3.2. Computational Domain and Mesh Details

For CFD simulations of the propeller model rotating in the uniform inflow, the computational domain was set up to include the static background region and the overset region, which included the propeller's rotation. In this study, the simulation domain was a 10D-diameter cylinder. The region size was determined to avoid block effects. On the four blade surfaces and the hub surface, a no-slip wall requirement was adopted.

Spatial discretization, an essential prerequisite for accurate numerical simulations, directly determines the quality of computational results. Unstructured grids exhibit a remarkable advantage in discretizing complex geometries. An unstructured grid was used to spatially discretize the computing domain. Special grid refinements were added to the whole computation discretization to improve the spatial resolution and better capture turbulence features in the propeller wake. Downstream, the axial length of the refining increased to 2.8D. Figure 2 depicts the propeller's mesh distribution with wake refinements. The LES approach needs $y+ < 1$ on the wall boundary and was fulfilled on the blades and hub. The computational domain consists of 48 million cells in total. The flow chart showing the modeling process of the CFD code is presented in Figure 3.
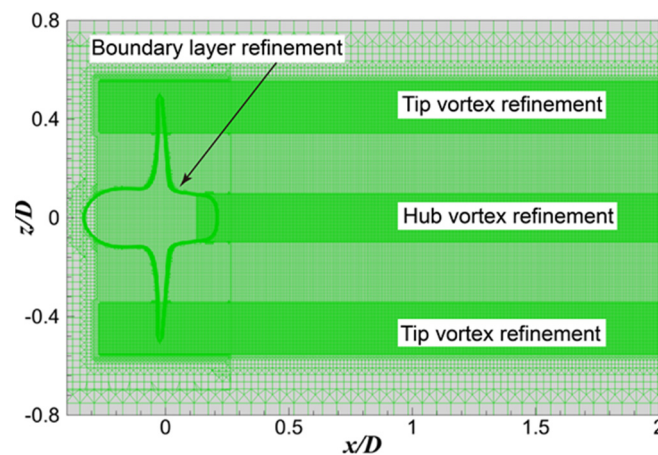
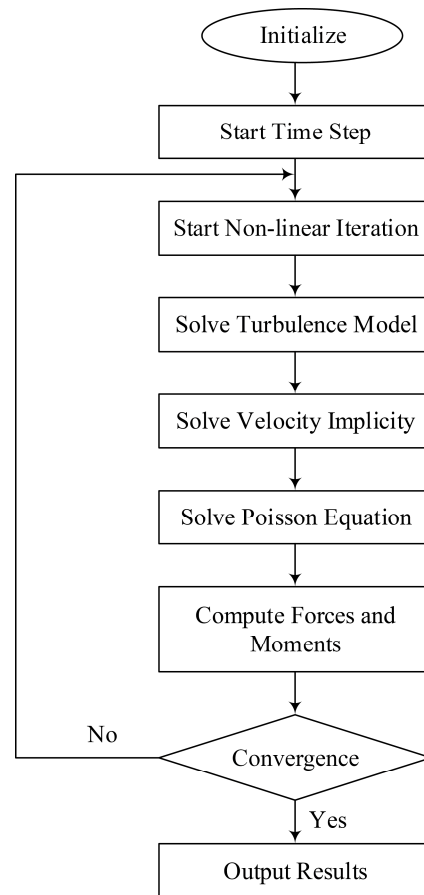**Figure 2.** Mesh distribution around the propeller with wake refinements.

Figure 3. A flow chart showing the modelling process.

3.3. Numerical Validation

The first step in numerical simulation is to validate the calculation results to make the research convincing. The most direct method is to compare it with relevant experimental results or previous calculations. To evaluate the correctness of the turbulence model and grid system utilized in this work, a comparison was performed between forces and moments and the wake field information produced by CFD simulations and the experimental

data available in the literature [32,33]. Three working conditions (J = 0.38, 0.748, and 0.88) were considered for numerical validation. Thrust and torque coefficients are defined as

$$K_t = \frac{T}{\rho n^2 D^4} \tag{5}$$

$$K_q = \frac{Q}{\rho n^2 D^5} \tag{6}$$

where T and Q are the propeller thrust and torque, respectively. ρ is the fluid density, n is the rotational speed of the propeller, and D is the propeller diameter. Figure 4a displays a comparison between the results obtained from experiments and CFD. The mean thrust and torque coefficients from numerical computations have small errors. However, it should be noted that under the heavy-loading condition, the CFD simulations tend to slightly overestimate the torque coefficient.
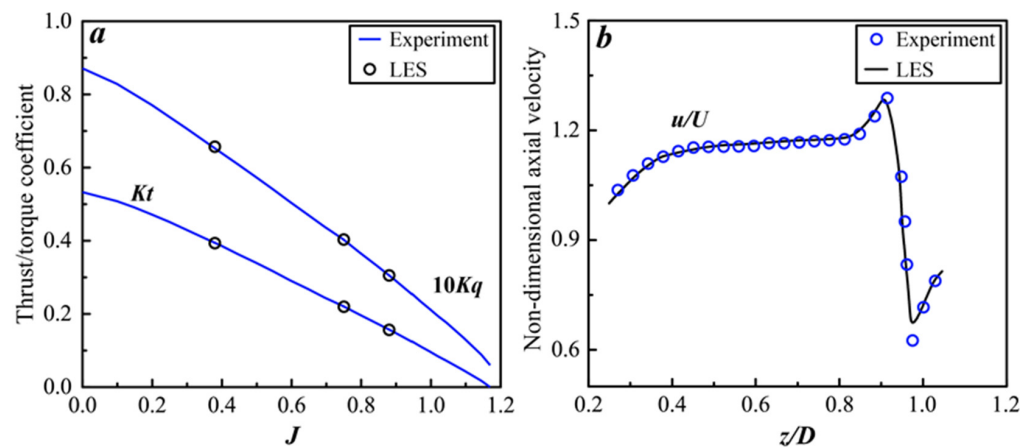

Figure 4. Validation analysis: (**a**) Open-water curves; (**b**) phase-averaged axial velocity.

The statistics of the phase average of the rotating machinery are computed as

$$\hat{f} = \frac{1}{m}\sum_{i=1}^{m} f\left(x, y, z, t_0 + \frac{i-1}{\epsilon n}\right) \tag{7}$$

Time-averaged statistics are computed as

$$<f> = \frac{1}{m}\sum_{i=1}^{m} f(x, y, z, t_i) \tag{8}$$

where m is the total number of instantaneous snapshots, ϵ is the number of propeller blades, n represents the propeller rotating speed, and t_0 indicates the moment when the sampling starts. The phase-averaged axial velocity profile was retrieved at x/D = 0.1 along the line. The agreement between the calculation and experiment is likewise excellent, as shown in Figure 4b.

The current numerical validation analysis shows that the mesh and numerical calculation method are good for the following exploration of propeller flows.

The two-grid evaluation approach [48,49] was used to evaluate grid convergence, with an emphasis on the thrust coefficients of the propeller. With a grid refinement ratio of 2, the researchers analyzed both fine and medium grids. The study's findings are reported in Table 2. Notably, the obtained UN (numerical uncertainty) values were less than 1.4% for the two loading situations analyzed. This result implies that the numerical approach and grid strategy used in this investigation are dependable.

Table 2. Grid convergence results.

Load	Medium	Fine	E	Extr.	UN (%)
$J = 0.38$					
Kt	0.4015	0.3969	4.6×10^{-3}	0.3923	1.17
$J = 0.65$					
Kt	0.273	0.2767	-3.7×10^{-3}	0.2804	1.32

4. Results and Analysis

CFD models rely largely on the local cell fluid velocity, which determines the non-dimensional distance between the wall and the first grid node. Figure 5 depicts the distribution of instantaneous wall $y+$ on propeller surfaces under various loading situations. The findings indicate that the value of $y+$ is always between 0 and 1, and that comparatively high values of $y+$ are dispersed at the blade tip areas, where considerable flow separation occurs, and tip vortices are prominently formed. Figure 5 also reveals that the $y+$ at the tip area is minimal for the mild-loading condition with relatively weak tip vortices, showing that the wall $y+$ grows as the loading condition increases. Generally speaking, the current near-wall resolution is enough for LES simulations.
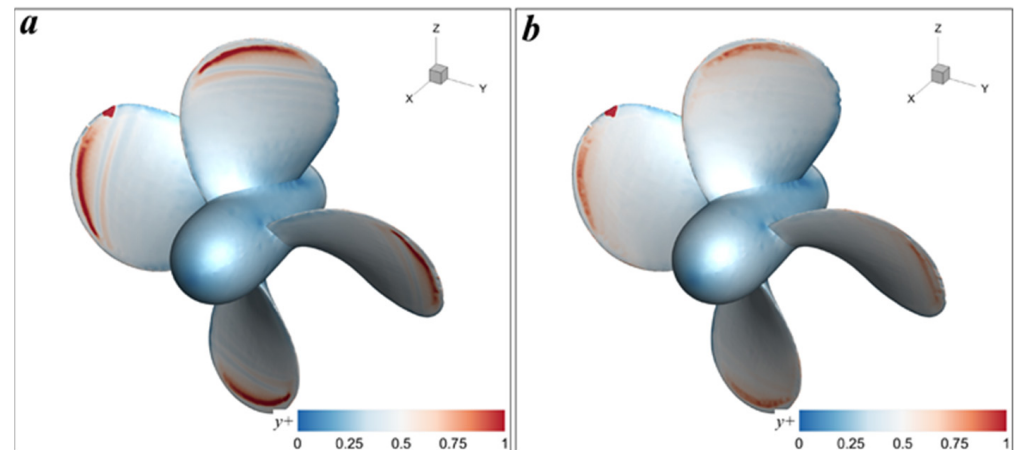

Figure 5. Instantaneous wall y+ distribution on propeller surfaces of (**a**) $J = 0.38$ and (**b**) $J = 0.65$, showing near-wall resolution in the CFD simulation.

To elucidate the turbulence characteristics in the propeller wakes, probe P1 is placed in the propeller wake to capture the time series of various velocity components. P1 is situated along the wake vortex trajectory in order to describe its features more accurately. Figure 6 depicts the power spectral density (PSD) of velocity components for probe P1 under various loading situations. The blade-passing frequency (f_{bp}) is used to scale the horizontal axis frequency. The dashed line represents the isotropic homogeneous turbulence of the Kolmogorov theory with a $-5/3$ slope. It can be seen from the figure that the current LES simulations capture the inertial range of frequencies well for both high and low-loading circumstances, demonstrating the numerical model and distribution are precise enough to capture the wake behaviors during the downstream evolution. Overall, the peaks are prominent for all velocity components under both loading situations, with the blade passage frequency being the dominating frequency, suggesting that the near-field wake vortices are coherent.
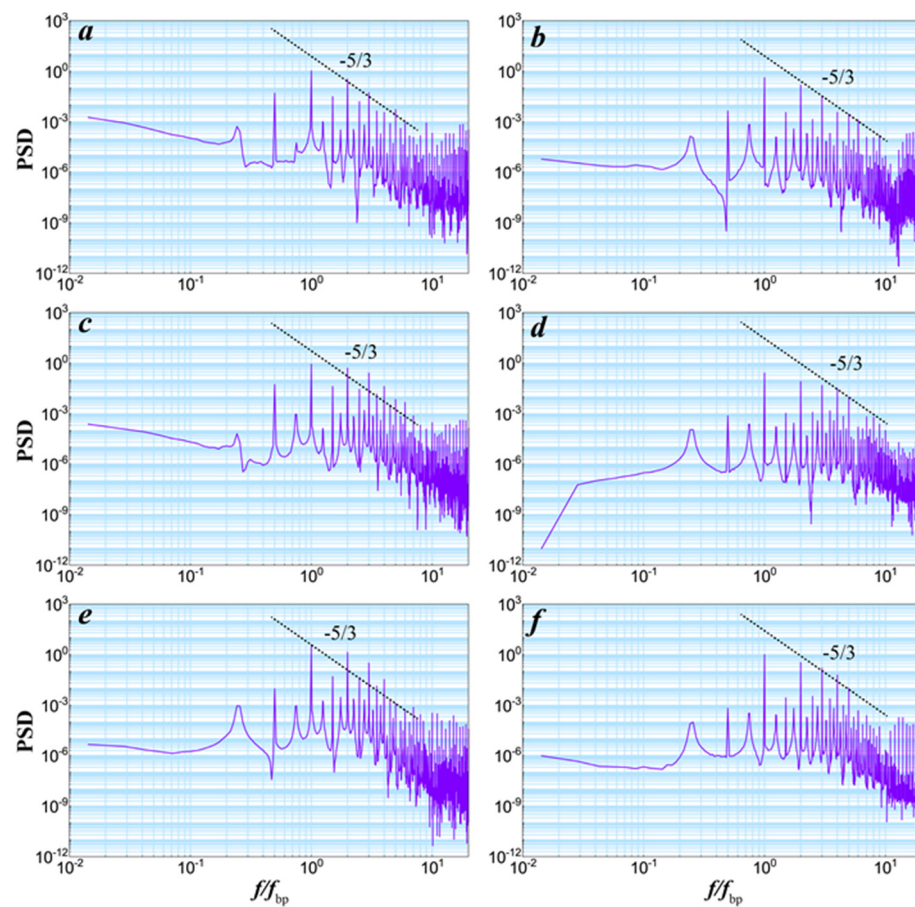
Figure 6. PSD of velocity components at probe P_1 for $J = 0.38$: (**a**) Streamwise velocity, (**c**) horizontal velocity, (**e**) vertical velocity; $J = 0.65$: (**b**) Streamwise velocity, (**d**) horizontal velocity, (**f**) vertical velocity.

The three-dimensional vortex structure can intuitively reflect the dynamic characteristics of the flow field. Figure 7 displays vortical structures of different loading conditions, with the wake vortex located at $y > 0$ blocked for visual clarity, which is represented using the iso-surface of Q-Criterion. Figure 7 shows that the wake vortex under high-loading circumstances is more complex than under light-loading conditions with the same Q-criterion value. Regardless of advance coefficients, the propeller wake recognizes the vortices with strong intensity. Vortices are very stable with coherence in the surrounding environment. As seen in Figure 7a, a significant elliptic instability (short-wave instability) forms on the helicoidal vortex in the middle field with the low advance coefficient, resulting in the formation of interlaced spirals as the flow progresses downstream. The secondary vortices and tangled spirals that link the neighboring tip vortices exacerbate the effects of mutual inductance. The propeller wake system loses coherence and breaks down, while the vortex is often evenly scattered. In contrast to the tip vortex, the hub vortex morphology is quite consistent. As for the condition with higher J, the vortex topology is quite simple with strong coherence, as presented in Figure 7b. Stable vortex structures can be observed in the near and middle fields. Elliptic instability and the pairing process occur in the further downstream wake. The convection velocity transferring tip vortices downstream is larger under the light-loading condition, which leads to the larger pitch of the helicoidal vortices. The larger pitch weakens the mutual inductance or interaction effects among tip vortices, which delays the instability behaviors of the whole vortex system.
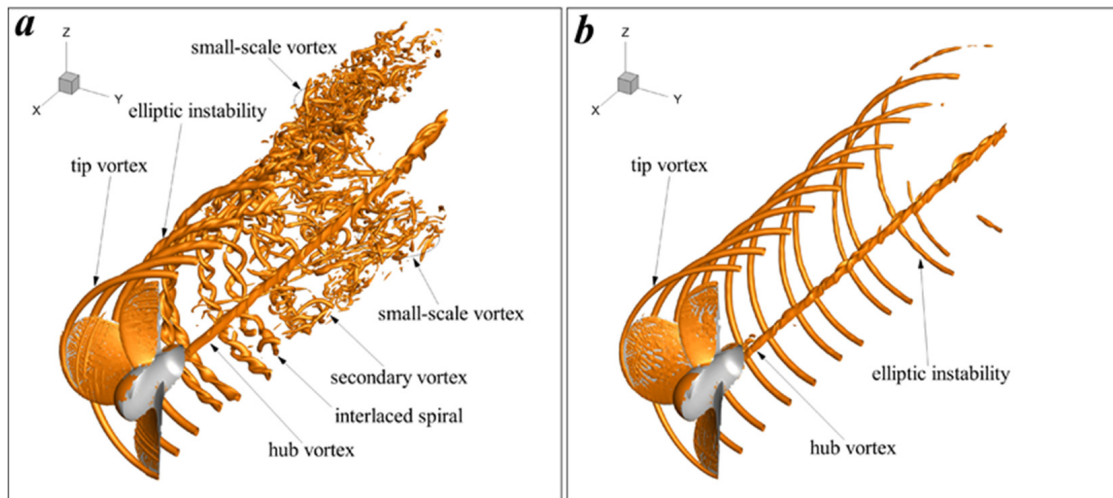
Figure 7. Three-dimensional vortical structures for (**a**) *J* = 0.38 and (**b**) *J* = 0.65.

Figure 8 illustrates the development of the wake by showing the instantaneous streamwise, horizontal, and vertical velocities for various advanced factors. The fundamental cause of the unstable wake fields is the velocity fields. Specifically, the propeller rotation accelerates the flow field behind the rotating propeller, which causes the wake to diminish in all fields of velocity components. Since convection velocity is greater in the former situation, it is possible to witness a more pronounced wake contraction under circumstances of heavy loading than under conditions of low loading. Additionally, it is evident from the horizontal velocity field that the propeller rotation has had a minor influence on the incoming flow. Indicated in the horizontal velocity field are the flow rotation rates induced by the propeller rotation. The interaction among neighboring tip vortices is reliant on azimuthal velocity diffusion, as shown by the vertical velocity fields. The increase in the axial velocity distribution with the inner radius position compared to the outer radius provides kinetic energy for the tip vortex pairing process.
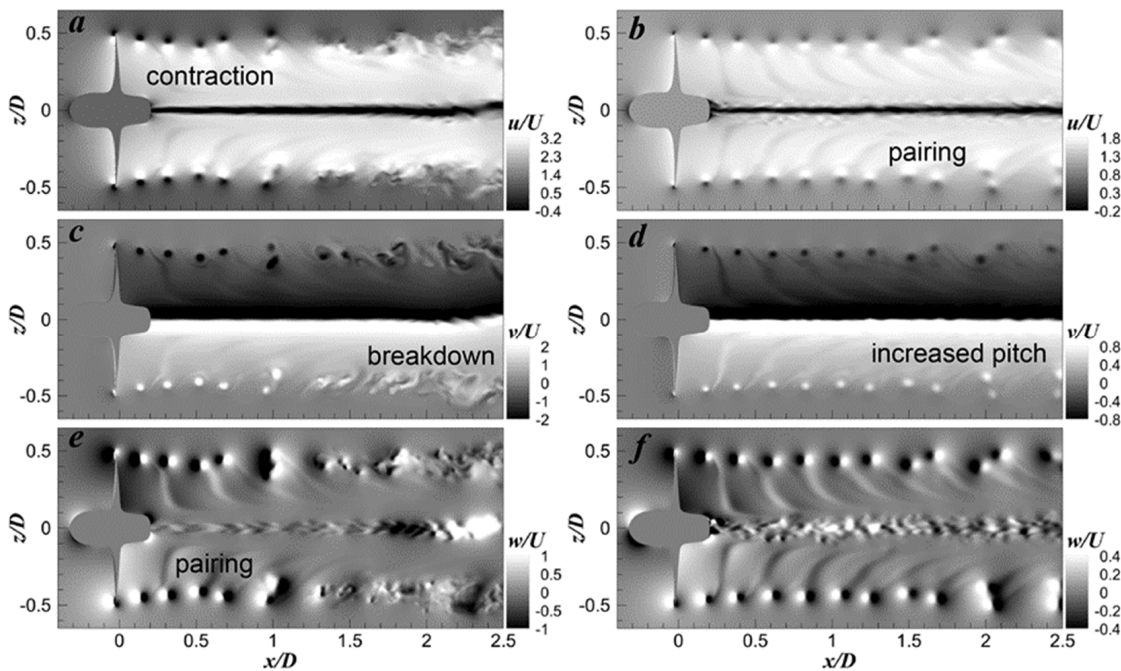

Figure 8. Instantaneous (**a**) streamwise velocity, (**c**) horizontal velocity, and (**e**) vertical velocity at *J* = 0.38 and (**b**) streamwise velocity, (**d**) horizontal velocity, and (**f**) vertical velocity at *J* = 0.65.

Figure 9 displays vorticity fields in the longitudinal plane under a range of loading conditions to study the flow physics associated with the wake instability further. Extreme loading conditions accentuate the visibility of tip vortices. Under circumstances of intense stress, when x/D is less than 0.5, tip vortices maintain a steady pitch, indicating that they are generally stable in this range. The merging of vortex pairs occurs at $x/D > 0$. when mutual induction between neighboring vortices intensifies. The upstream and downstream vortices converge in the streamwise direction to produce vortex pairs. When $x/D > 1.2$, under the impact of enhanced elliptic instability, the vortex pair disintegrates into smaller-scale vortex forms. At $x/D > 2$, the wake system decomposes into homogeneous vortices, and at the same time, the hub vortex begins to lose coherence concurrently. In the low-loading condition with $J = 0.65$, the vortices are equally spaced, suggesting a stable topology of the vortex system. The merging of vortices starts when $x/D > 1.5$, resulting in two vortex pairs with an increased pitch. The evolution of tip vortices is very consistent with the law of turbulence evolution, in which large vortices evolve into small vortices, accompanied by turbulence mixing and energy dissipation, and this process is accelerated by the instability motion of the vortex system.
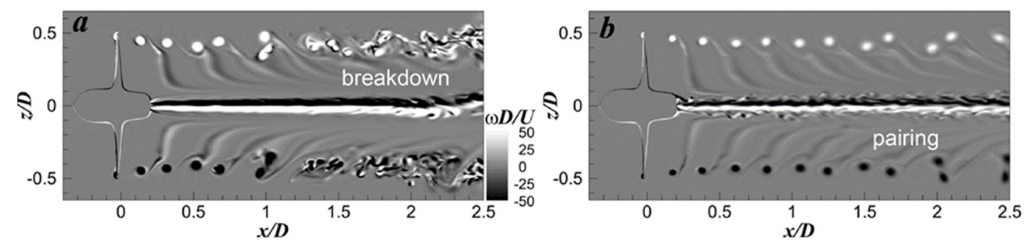

Figure 9. Instantaneous out-of-plane vorticity at (**a**) $J = 0.38$ and (**b**) $J = 0.65$.

Some important flow field characteristics can also be obtained from the perspective of time-averaged statistics. The time-averaged characteristics of physical quantities can reflect the overall flow behaviors. Figure 10 depicts the time-averaged axial velocity and pressure fields under different loading conditions. In places where the propeller blades generate the maximum thrust, the highest velocities are also attained. In the mutual inductance-generated pairing process, the envelope of the mean axial velocity depicts unstable motion. The region of low velocity near the envelope's edge exemplifies the mutual induction of adjacent tip vortices. The expansion of the central low-velocity zone in the axial velocity field indicates a more coherent hub vortex under light-loading circumstances.
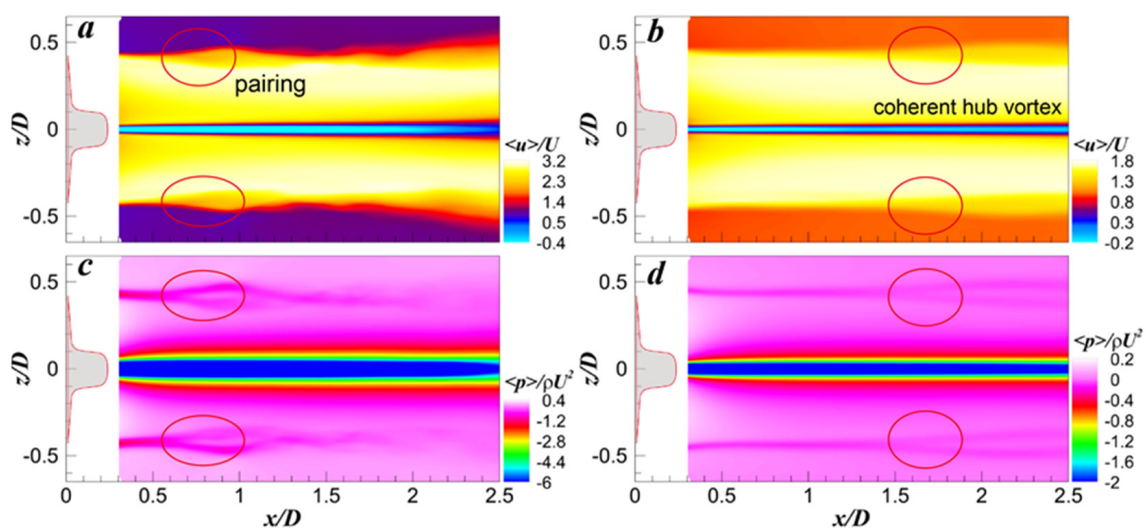

Figure 10. Time-averaged contours of (**a**) streamwise velocity and (**c**) pressure for $J = 0.38$ and (**b**) streamwise velocity and (**d**) pressure for $J = 0.65$.

The mean pressure fields clearly depict the paths of the tip vortex evolution, as well as the onset of vortex instability and pairing. The pairing behavior is delayed when the advance coefficient is rather large.

Figure 11 depicts the spectra of the time-averaged streamwise velocity for different propeller loads. The spectra of the streamwise velocity are recovered at positions $x/D = 0.5$ and 2 downstream. Normalization of velocities is performed using the inflow velocity. As seen in Figure 10, the flow acceleration area can be characterized by the axial velocity, which is responsible for the velocity peaks shown in the figure. The hub wake causes the middle maximum of the velocity profiles. Consistent with the behavior seen in Figure 9, the vortex strength decreases as the advance coefficient rises. In addition, the viscous diffusion effects can be deduced from the streamwise velocity profiles, which are most significant in the hub vortex region, where the peak values decrease as the vortex system evolves downstream. The gradient of the mean velocity in the tip vortex region also decreases as the vortex system moves downstream, indicating that the vortex strength weakens during the evolution process.
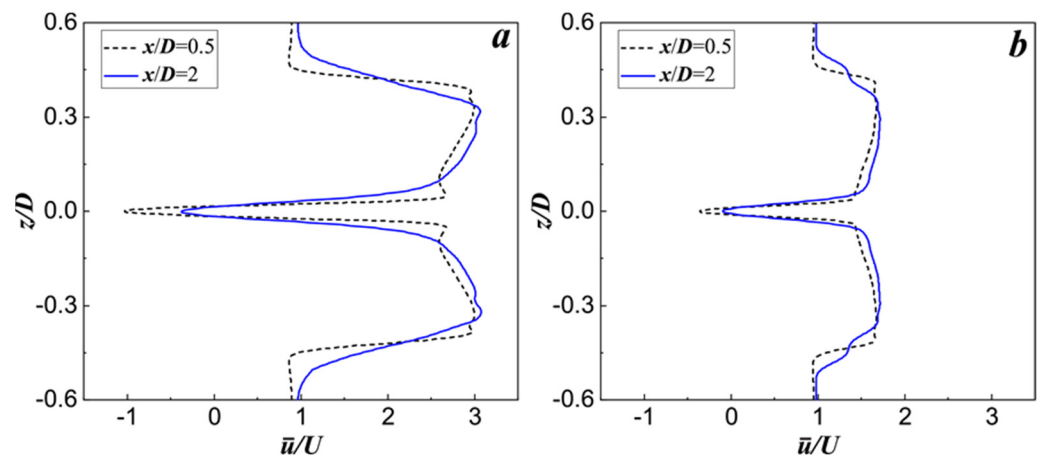

Figure 11. Profiles of the time-averaged streamwise velocity for different downstream locations at (**a**) $J = 0.38$ and (**b**) $J = 0.65$.

5. Conclusions

The macroscopic performances of a propeller are often determined by its interaction with the surrounding fluid. Studying the macro performance of a propeller from the perspective of fine flow fields can help people deeply understand the essential factors that change propeller performance. Because of their relationship to noise, vibration, and mechanical concerns, the propeller's wake development characteristics are of great interest. On inland rivers and in deep-sea waterways, propellers are the major propulsion devices for boats. In this work, the fundamental mechanisms governing propeller wake formation were investigated, with a focus on the events related to the start of instability. From several perspectives, the development features of the vortex system topology were characterized. According to the statistics, the greatest streamwise velocity is reached in places where the propeller blades provide the highest thrust. With the increase in the advance coefficient, due to the greater convection velocity in situations of high loading, the shrinkage of the wake is more pronounced under these conditions than under conditions of low loading. Under high stress levels, the vortex system has a complex shape, but under light-loading conditions, the wake vortex system is simpler and more coherent.

This study contributes to our comprehension of propeller wake instability processes under varied loads. The findings and conclusions of this study have the potential to inform the optimization of aquaculture support vessel propellers in the future.

The current work only considers the case of uniform inflow; however, propellers always work in more complex environments in engineering practice. More complex inflow conditions need to be considered when studying the propeller wake instabilities in future

work. In addition, to understand the complete evolution process of the propeller wake, the vortex structures at a further distance downstream of the propeller should be captured in numerical simulations.

Institutional Review Board Statement: Not applicable.

Informed Consent Statement: Not applicable.

Data Availability Statement: The data that support the findings of this study are available within the article.

Conflicts of Interest: The authors declare no conflict of interest.

References

1. Deng, R.; Zhang, Z.; Luo, F.; Sun, P.; Wu, T. Investigation on the Lift Force Induced by the Interceptor and Its Affecting Factors: Experimental Study with Captive Model. *J. Mar. Sci. Eng.* **2022**, *10*, 211. [CrossRef]
2. Wang, L.Z.; Guo, C.Y.; Su, Y.M.; Wu, T.C. A numerical study on the correlation between the evolution of propeller trailing vortex wake and skew of propellers. *Int. J. Nav. Archit. Ocean. Eng.* **2018**, *10*, 212–224. [CrossRef]
3. Sasmal, A.; De, S. Wave interaction with a pair of thick barriers over a pair of trenches. *Ships Offshore Struct.* **2022**, *17*, 2031–2044. [CrossRef]
4. Das, A.; De, S.; Mandal, B.N. Radiation of water waves by a heaving submerged disc in a three-layer fluid. *J. Fluids Struct.* **2022**, *111*, 103575. [CrossRef]
5. Sasmal, A.; De, S. Energy dissipation and oblique wave diffraction by three asymmetrically arranged porous barriers. *Ships Offshore Struct.* **2022**, *17*, 105–115. [CrossRef]
6. Sun, C.; Wang, L. Modal analysis of propeller wake dynamics under different inflow conditions. *Phys. Fluids* **2022**, *34*, 125109. [CrossRef]
7. Wang, H.; Hou, Y.; Xiong, Y.; Liang, X. Research on multi-interval coupling optimization of ship main dimensions for minimum EEDI. *Ocean Eng.* **2021**, *237*, 109588. [CrossRef]
8. Di Mascio, A.; Dubbioso, G.; Muscari, R. Vortex structures in the wake of a marine propeller operating close to a free surface. *J. Fluid Mech.* **2022**, *949*, A33. [CrossRef]
9. Zhao, D.; Guo, C.; Su, Y.; Wang, L.; Wang, C. Numerical study on the unsteady hydrodynamic performance of a four-propeller propulsion system undergoing oscillatory motions. *J. Coast. Res.* **2017**, *33*, 347–358. [CrossRef]
10. Sun, P.; Pan, L.; Liu, W.; Zhou, J.; Zhao, T. Wake Characteristic Analysis of a Marine Propeller under Different Loading Conditions in Coastal Environments. *J. Coast. Res.* **2022**, *38*, 613–623. [CrossRef]
11. Zhou, J.; Sun, P.; Pan, L. Modal Analysis of the Wake Instabilities of a Propeller Operating in Coastal Environments. *J. Coast. Res.* **2022**, *38*, 1163–1171. [CrossRef]
12. Felli, M. Underlying mechanisms of propeller wake interaction with a wing. *J. Fluid Mech.* **2021**, *908*, A10. [CrossRef]
13. Capone, A.; Di Felice, F.; Pereira, F.A. On the flow field induced by two counter-rotating propellers at varying load conditions. *Ocean Eng.* **2021**, *221*, 108322. [CrossRef]
14. Wang, L.; Guo, C.; Wang, C.; Xu, P. Modified phase average algorithm for the wake of a propeller. *Phys. Fluids* **2021**, *33*, 035146. [CrossRef]
15. de Vries, R.; van Arnhem, N.; Sinnige, T.; Vos, R.; Veldhuis, L.L. Aerodynamic interaction between propellers of a distributed-propulsion system in forward flight. *Aerosp. Sci. Technol.* **2021**, *118*, 107009. [CrossRef]
16. Wang, L.; Martin, J.E.; Felli, M.; Carrica, P.M. Experiments and CFD for the propeller wake of a generic submarine operating near the surface. *Ocean Eng.* **2020**, *206*, 107304. [CrossRef]
17. Posa, A.; Broglia, R.; Felli, M.; Falchi, M.; Balaras, E. Characterization of the wake of a submarine propeller via large-eddy simulation. *Comput. Fluids* **2019**, *184*, 138–152. [CrossRef]
18. Posa, A.; Broglia, R. Near wake of a propeller across a hydrofoil at incidence. *Phys. Fluids* **2022**, *34*, 065141. [CrossRef]

19. Posa, A.; Broglia, R.; Balaras, E. The dynamics of the tip and hub vortices shed by a propeller: Eulerian and Lagrangian approaches. *Comput. Fluids* **2022**, *236*, 105313. [CrossRef]
20. Shi, H.; Wang, T.; Zhao, M.; Zhang, Q. Modal analysis of non-ducted and ducted propeller wake under axis flow. *Phys. Fluids* **2022**, *34*, 055128. [CrossRef]
21. Qin, D.; Huang, Q.; Pan, G.; Chao, L.; Luo, Y.; Han, P. Effect of the odd and even number of blades on the hydrodynamic performance of a pre-swirl pumpjet propulsor. *Phys. Fluids* **2022**, *34*, 035120. [CrossRef]
22. Wang, L.; Liu, X.; Wu, T. Modal analysis of the propeller wake under the heavy loading condition. *Phys. Fluids* **2022**, *34*, 055107. [CrossRef]
23. Wang, L.; Liu, X.; Wang, N.; Li, M. Modal analysis of propeller wakes under different loading conditions. *Phys. Fluids* **2022**, *34*, 065136. [CrossRef]
24. Li, H.; Huang, Q.; Pan, G.; Dong, X. Wake instabilities of a pre-swirl stator pump-jet propulsor. *Phys. Fluids* **2021**, *33*, 085119. [CrossRef]
25. Qin, D.; Huang, Q.; Pan, G.; Han, P.; Luo, Y.; Dong, X. Numerical simulation of vortex instabilities in the wake of a preswirl pumpjet propulsor. *Phys. Fluids* **2021**, *33*, 055119. [CrossRef]
26. Wang, L.; Carrica, P.M.; Felli, M. Experimental and CFD Study of the Streamwise Evolution of Propeller Tip Vortices. In Proceedings of the 33rd Symposium on Naval Hydrodynamics, Osaka, Japan, 18–23 October 2020; pp. 1–18.
27. Muscari, R.; Di Mascio, A.; Verzicco, R. Modeling of vortex dynamics in the wake of a marine propeller. *Comput. Fluids* **2013**, *73*, 65–79. [CrossRef]
28. Di Mascio, A.; Muscari, R.; Dubbioso, G. On the wake dynamics of a propeller operating in drift. *J. Fluid Mech.* **2014**, *754*, 263–307. [CrossRef]
29. Li, H.; Huang, Q.; Pan, G.; Dong, X.; Li, F. An investigation on the flow and vortical structure of a pre-swirl stator pump-jet propulsor in drift. *Ocean Eng.* **2022**, *250*, 111061. [CrossRef]
30. Chen, G.; Li, X.B.; Liang, X.F. IDDES simulation of the performance and wake dynamics of the wind turbines under different turbulent inflow conditions. *Energy* **2022**, *238*, 121772. [CrossRef]
31. Wang, L.; Wu, T.; Gong, J.; Yang, Y. Numerical simulation of the wake instabilities of a propeller. *Phys. Fluids* **2021**, *33*, 125125. [CrossRef]
32. Di Felice, F.; Di Florio, D.; Felli, M.; Romano, G.P. Experimental investigation of the propeller wake at different loading conditions by particle image velocimetry. *J. Ship Res.* **2004**, *48*, 168–190. [CrossRef]
33. Salvatore, F.; Testa, C.; Ianniello, S.; Pereira, F. Theoretical modelling of unsteady cavitation and induced noise. In Proceedings of the CAV 2006 Symposium, Wageningen, The Netherlands, 11–15 September 2006; pp. 1–13.
34. Sezen, S.; Cosgun, T.; Yurtseven, A.; Atlar, M. Numerical investigation of marine propeller underwater radiated noise using acoustic analogy Part 2: The influence of eddy viscosity turbulence models. *Ocean Eng.* **2021**, *220*, 108353. [CrossRef]
35. Wang, L.; Guo, C.; Su, Y.; Xu, P.; Wu, T. Numerical analysis of a propeller during heave motion in cavitating flow. *Appl. Ocean Res.* **2017**, *66*, 131–145. [CrossRef]
36. Wang, L.; Guo, C.; Xu, P.; Su, Y. Analysis of the performance of an oscillating propeller in cavitating flow. *Ocean Eng.* **2018**, *164*, 23–39. [CrossRef]
37. Wang, L.; Guo, C.; Xu, P.; Su, Y. Analysis of the wake dynamics of a propeller operating before a rudder. *Ocean Eng.* **2019**, *188*, 106250. [CrossRef]
38. Wang, L.; Wu, T.; Gong, J.; Yang, Y. Numerical analysis of the wake dynamics of a propeller. *Phys. Fluids* **2021**, *33*, 095120. [CrossRef]
39. Posa, A.; Balaras, E. A numerical investigation of the wake of an axisymmetric body with appendages. *J. Fluid Mech.* **2016**, *792*, 470–498. [CrossRef]
40. Wang, C.; Li, P.; Guo, C.; Wang, L.; Sun, S. Numerical research on the instabilities of CLT propeller wake. *Ocean Eng.* **2022**, *243*, 110305. [CrossRef]
41. Kumar, P.; Mahesh, K. Large eddy simulation of propeller wake instabilities. *J. Fluid Mech.* **2017**, *814*, 361–396. [CrossRef]
42. Andredaki, M.; Georgoulas, A.; Marengo, M. Numerical investigation of quasi-sessile droplet absorption into wound dressing capillaries. *Phys. Fluids* **2020**, *32*, 092112. [CrossRef]
43. Nguyen, V.B.; Do, Q.V.; Pham, V.S. An OpenFOAM solver for multiphase and turbulent flow. *Phys. Fluids* **2020**, *32*, 043303. [CrossRef]
44. Wang, L.; Guo, C.; Wan, L.; Su, Y. Numerical analysis of propeller during heave motion near a free surface. *Mar. Technol. Soc. J.* **2017**, *51*, 40–51.
45. Wang, L.; Guo, C.; Su, Y.; Wu, T.; Wang, S. Numerical study of the viscous flow field mechanism for a non-geosim model. *J. Coast. Res.* **2017**, *33*, 684–698.
46. Wang, L.; Guo, C.; Su, Y.; Zhang, D. Numerical study of the propeller-induced exciting force under the open freedom condition. *J. Harbin Eng. Univ.* **2017**, *38*, 822–828.
47. Wang, L.; Guo, C.; Su, Y. Numerical analysis of flow past an elliptic cylinder near a moving wall. *Ocean Eng.* **2018**, *169*, 253–269. [CrossRef]

48. Gong, J.; Ding, J.; Wang, L. Propeller–duct interaction on the wake dynamics of a ducted propeller. *Phys. Fluids* **2021**, *33*, 074102. [CrossRef]

49. Roache, P.J. Quantification of uncertainty in computational fluid dynamics. *Annu. Rev. Fluid Mech.* **1997**, *29*, 123–160. [CrossRef]